J Nanostruct 15(3): 1025-1033, Summer 2025

RESEARCH PAPER

Electronic and Structural Elucidation of ZnO-ZnS–Aniline Nanocomposite Interactions via DFT and Microscopy Techniques

*Uday Abdul-Reda Hussein [1], Usama S. Altimari [2], Fadhil M. Abid [3], Shaima Abd [4], Aseel M. Aljeboree [5], Ayad F. Alkaim [5]**

[1] *Department of pharmaceutics, College of Pharmacy, University of Al-Ameed, Iraq*
[2] *Department of Medical Laboratories Technology, AL-Nisour University College, Baghdad, Iraq*
[3] *Al-Hadi University College, Baghdad, 10011, Iraq*
[4] *Department of Sciences, Al-Manara College for Medical Sciences, Maysan, Iraq*
[5] *Department of Chemistry, College of Science for Women, University of Babylon, Iraq*

ARTICLE INFO

Article History:
Received 22 April 2025
Accepted 26 June 2025
Published 01 July 2025

Keywords:
DFT
Nanocomposites
RDG isosurfaces
XRD

ABSTRACT

Nanostructured surfaces are notable for diverse applications like molecular adsorption. Here, we utilize density functional theory (DFT) to explore the adsorption characteristics of aniline on a hybrid ZnO/ZnS cluster. To clarify the interaction's nature, we performed a comprehensive analysis using Quantum Theory of Atoms in Molecules (QTAIM), Electrostatic Potential (ESP), Electron Localization Function (ELF), Non-Covalent Interaction (NCI) analysis via Reduced Density Gradient (RDG) and sign(λ_2)•ρ plots, along with Frontier Molecular Orbital (FMO) analysis. The QTAIM analysis revealed the presence of a bond critical point (BCP) between aniline's nitrogen atom and a zinc atom on the surface. The electron density (ρ) at this point was measured to be 0.075341 a.u., with a Laplacian ($\nabla^2\rho$) of +0.278076 a.u., suggesting a non-covalent, closed-shell interaction. ESP mapping revealed a distinct electrostatic complementarity between the nitrogen atom of aniline, with high electron density, and the electron-poor zinc sites on the surface. ELF analysis indicated a partial delocalization of the nitrogen lone pair upon adsorption, which implies a redistribution of electron density. NCI analysis primarily identified van der Waals interactions. RDG isosurfaces highlighted areas of weak attractive forces, which were supported by sign(λ_2)•ρ values. FMO analysis showed a decrease in the HOMO–LUMO gap from 5.44 eV for isolated aniline to 2.74 eV for the composite sample, indicating a greater electronic interaction and the possibility of charge transfer.

How to cite this article
Hussein U., Altimari U., Abid F., Abd S., Aljeboree A., Alkaim A. Electronic and Structural Elucidation of ZnO-ZnS–Aniline Nanocomposite Interactions via DFT and Microscopy Techniques. J Nanostruct, 2025; 15(3):1025-1033. DOI: 10.22052/JNS.2025.03.019

INTRODUCTION

The organic compound-based semiconductor surfaces are a cornerstone of many technologies, such as chemical sensors, photocatalysis, and the creation of electronic devices. A deep understanding of these interactions at a molecular scale is essential for the intelligent design of advanced materials [1-4]. Aniline, a basic aromatic amine, provides a useful model for exploring how π-conjugated systems interact with semiconductor

* *Corresponding Author Email: alkaimayad@gmail.com*

surfaces. The nitrogen atom's lone electron pair, along with delocalized π-electron system, makes aniline well-suited for investigating adsorption behaviors. Zinc oxide (ZnO) and zinc sulfide (ZnS) are II–VI semiconductors characterized by their large band gaps and are widely researched for their electronic and optical characteristics. The creation of ZnO/ZnS heterostructures has attracted considerable interest due to their improved photocatalytic performance and adjustable electronic characteristics, positioning them for use in diverse applications, including sensors and optoelectronic components [5-7]. Prior research utilizing Density Functional Theory (DFT) has investigated the adsorption of organic molecules on both ZnO and ZnS surfaces, yielding valuable data regarding adsorption energies, charge transfer phenomena, and alterations in electronic structure. Nevertheless, a investigation incorporating topological, electrostatic, and orbital viewpoints is still lacking [8-10]. In this study, we undertake a comprehensive DFT analysis of aniline adsorption on a ZnO-ZnS hybrid cluster. Through the application of Quantum Theory of Atoms in Molecules (QTAIM), Electrostatic Potential (ESP), Electron Localization Function (ELF), Non-Covalent Interactions (NCI), and Frontier Molecular Orbital (FMO) analyses, we clarify the characteristics of the interaction, the redistribution of electron density, and the resulting effects on the electronic properties of the hybrid system. This diverse methodology offers a complete comprehension of the adsorption process, thereby enriching the broader understanding of organic–inorganic interface chemistry.

MATERIALS AND METHODS

Preparation of ZnO-ZnS nanocomposites

According to the previous work [11], a hydrothermal methodology was employed to synthesize the target materials. Initially, 0.1 mol of zinc chloride ($ZnCl_2$) was introduced into 20 mL of distilled water and subjected to continuous agitation for 1 h. The pH level of the resulting solution was carefully regulated through the gradual addition of sodium hydroxide (NaOH) solution. Following complete dissolution of the zinc chloride, the solution was transferred to a Teflon beaker, which was subsequently sealed within a 50 mL capacity autoclave. This autoclave was then maintained at a temperature of 150 °C for 3 h. In a separate procedure for the synthesis of ZnS, zinc chloride ($ZnCl_2$) and sodium sulfide (Na_2S) were combined in a 1:1 molar ratio and dissolved in 20 mL of distilled water. This mixture was also continuously stirred for 1 h. Upon complete dissolution, this solution was transferred to a Teflon beaker and sealed in a 50 mL autoclave. This autoclave was heated at 160 °C for 12 h. Following the hydrothermal treatment, both autoclaves were allowed to cool naturally to ambient temperature. The resulting precipitates from each reaction were then collected and subjected to repeated washing cycles using both water and ethanol. Finally, the washed precipitates were dried at 60 °C to obtain the final products.

Computational Details

All geometry optimizations and wavefunction analyses were performed using Gaussian 16 (Rev. C.01) with the B3LYP functional and a 6-31G(d,p) basis set for all non-metal atoms. For Zn and S, the LANL2DZ pseudopotential was applied to account for relativistic effects. The optimized structures were verified as minima *via* harmonic frequency analysis (no imaginary frequencies).

The wavefunction outputs were post-processed using Multiwfn 3.8 to perform:

- QTAIM analysis: for investigation of bond critical points (BCPs), atomic charges, and delocalization indices;
- ESP maps: for investigation of charge distribution and electrostatic complementarity;
- ELF analysis: for investigation of regions of localized electron density and lone pair participation;
- NCI analysis: using reduced density gradient (RDG) and sign(λ_2)·ρ plots to classify van der Waals and donor–acceptor interactions;
- HOMO–LUMO visualization and energy analysis: for examination of orbital alignment and interfacial charge transfer potential.

All visualizations were rendered using VMD 1.9.2 and VESTA 3.5.8.

RESULTS AND DISCUSSION

Structural and morphological characterization

The crystalline structure of the ZnO-ZnS nanocomposite was characterized using X-ray diffraction (XRD), and the pattern is shown in Fig. 1a. The diffraction peaks are observed at 2θ values of 18.81°, 22.02°, 24.41°, 28.94°, 32.06°, 35.06°, 38.06°, and 55.51°, corresponding to the reflection planes (111), (100), (002), (101), (102/220),

(110/311), (103), and (112), respectively. These reflections indicate the presence of both hexagonal wurtzite ZnO (JCPDS No. 36-1451) and cubic ZnS (JCPDS No. 05-0566) phases. The distinct and sharp peaks reflect the good crystallinity of the synthesized nanocomposite. Notably, the coexistence of ZnO and ZnS phases in the XRD pattern confirms the successful formation of a heterostructured composite, which is essential for achieving enhanced charge separation and optical performance [12].The broadening of the peaks is also indicative of the nanocrystalline nature, which is further confirmed by electron microscopy results. The SEM image (Fig. 1b) provides further insight into the surface morphology and microstructure of the ZnO-ZnS composite. The surface appears to be uniformly covered by densely packed, quasi-spherical nanoparticles, forming a continuous porous network. This microstructure favors surface adsorption and electron mobility by offering high surface area and effective interfacial contact between ZnO and ZnS grains. Moreover, the absence of large particle agglomerates indicates good dispersion and control over particle growth during synthesis. These features are beneficial for heterojunction-based applications, where charge separation and transport depend on the intimate contact between different semiconductor phases [13]. The combined XRD, TEM, and SEM analyses confirm the successful synthesis of a well-crystallized ZnO/ZnS nanocomposite, exhibiting: coexisting crystalline phases of ZnO and ZnS, nanoparticle morphology with uniform size distribution (~100 nm or smaller), surface roughness and porosity advantageous for molecular adsorption. TEM micrograph (Fig. 1c) reveals the presence of aggregated nanoparticle clusters with an average particle size below 100 nm. The particles appear spherical, with some degree of overlap and surface contact, which is favorable for producing interfacial heterojunctions between ZnO and ZnS domains. The visible contrast between darker and lighter regions may indicate different compositions (i.e., ZnO-rich vs ZnS-rich regions), highlighting the phase coexistence observed in the XRD results [10]. The nanometric dimensions observed in TEM support the XRD conclusion regarding the small crystallite size and confirm the suitability of the material for applications requiring high surface-to-volume ratios, such as adsorption, catalysis, or surface functionalization. These structural attributes make the material an excellent candidate for surface-sensitive applications, including chemical sensing and catalysis, which is consistent with its interaction characteristics

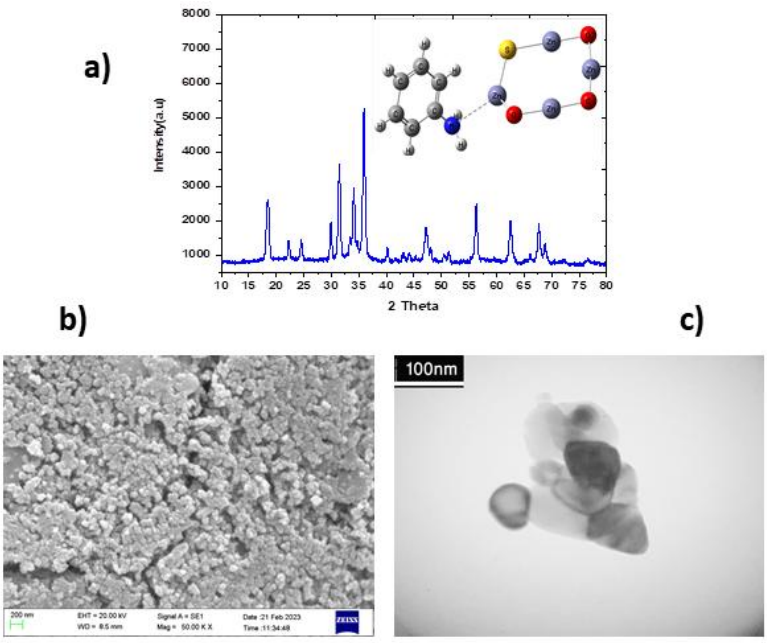

Fig. 1. (a) XRD pattern, (b) SEM and (c) TEM images of ZnO-ZnS nanocomosites.

observed in your quantum chemical analyses (ESP, QTAIM, NCI, etc.).

ESP and ELF analysis

The ESP distribution was calculated for the ZnO-ZnS–aniline hybrid system and visualized using dual isosurfaces at (±0.002 a.u.). The red isosurface corresponds to regions of negative ESP (electron-rich), while the yellow isosurface highlights positive ESP (electron-poor) zones as shown in Fig. 2a. ESP maps are powerful tools for identifying reactive sites, understanding molecular interactions, and predicting non-covalent bonding behavior[14]. The nitrogen atom in the aniline's $–NH_2$ group is within a negative ESP zone, as shown in Fig. 2a, confirming its lone pair's role as an electron donor. Zn atoms are surrounded by positive ESP, indicating Lewis acidic character and supporting the possibility of N→Zn donor–acceptor interaction [15]. The π-system of the aromatic ring contributes to a delocalized, slightly negative ESP region, allowing for π–metal interactions [15]. The complementary nature of ESP regions between the adsorbate and surface supports a stable, electrostatically driven adsorption mechanism.

The ELF was computed to assess electron pairing and bond localization within the composite. Isosurfaces at an ELF value of 0.80 a.u. were visualized, as illustrated in Fig. 2b. ELF is a quantum-topological descriptor widely used to reveal bonding character and electron pairing in molecules and solids [16]. Donut-shaped ELF lobes over the aromatic ring are consistent with π-electron delocalization. The $–NH_2$ group exhibits pronounced ELF near nitrogen, confirming the presence of a localized lone pair [17]. Surface oxygen and sulfur atoms show localized ELF regions, while Zn atoms lack ELF features, reflecting their role as electron acceptors. The ELF results validate the ESP-derived conclusion: no covalent bonding is observed, but directional electrostatic stabilization via localized donor–acceptor interactions dominates the adsorption process.

NCI and RDG analyses

To further investigate the nature of the interaction between aniline and the ZnO-ZnS surface, a NCI analysis was performed using the RDG approach implemented *via* Multiwfn and visualized with VMD. This method, developed by Johnson et al.[18], enables visualization of weak interactions in real space and provides insight into their nature—whether dispersive, attractive, or repulsive. The RDG scatter plot (Fig. 3a) provides a quantitative distribution of interaction types: The sharp peak near $\text{sign}(\lambda_2)\cdot\rho \approx 0$ corresponds to dispersion interactions, affirming the dominance of van der Waals contacts in the system. The blue shoulder extending into negative $\text{sign}(\lambda_2)\cdot\rho$ values (~ –0.02 to –0.03 a.u.) confirms the presence of moderate attractive interactions, such as N···Zn electrostatic coordination [18, 19]. A small population at positive $\text{sign}(\lambda_2)\cdot\rho$ indicates repulsive contacts, but their relative weakness suggests that they do not hinder overall complex stability. Fig. 3b shows the NCI isosurface of the ZnO-ZnS–aniline,

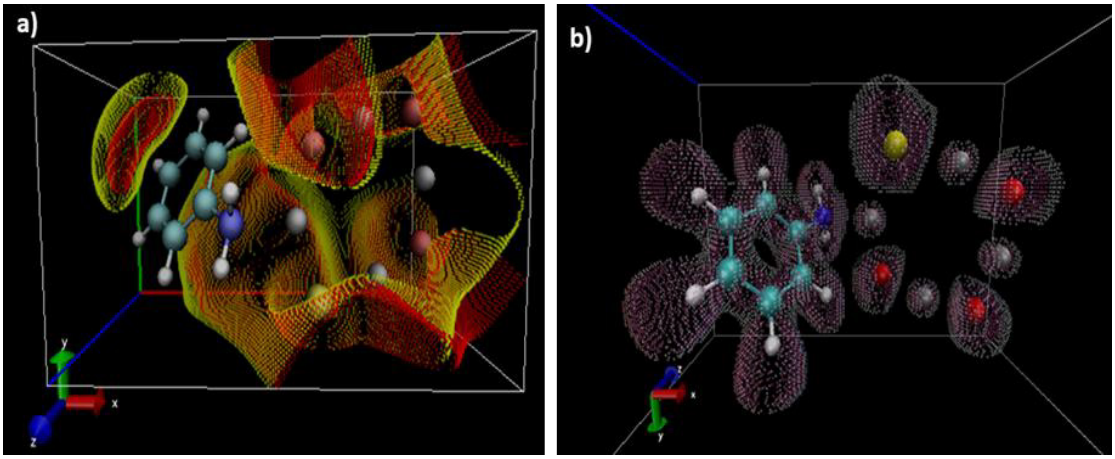

Fig. 2. (a) ESP and (b) ELF for aniline interaction with ZnO-ZnS nanosurface.

mapped at an RDG value of 0.5 a.u. and color-coded by sign(λ_2)·ρ. This descriptor combines the electron density (ρ) and the second eigenvalue (λ_2) of the Hessian matrix of the electron density to classify interaction types: Green isosurfaces indicate van der Waals (vdW) interactions, which are weak and non-directional. These interactions are broadly distributed along the contact region

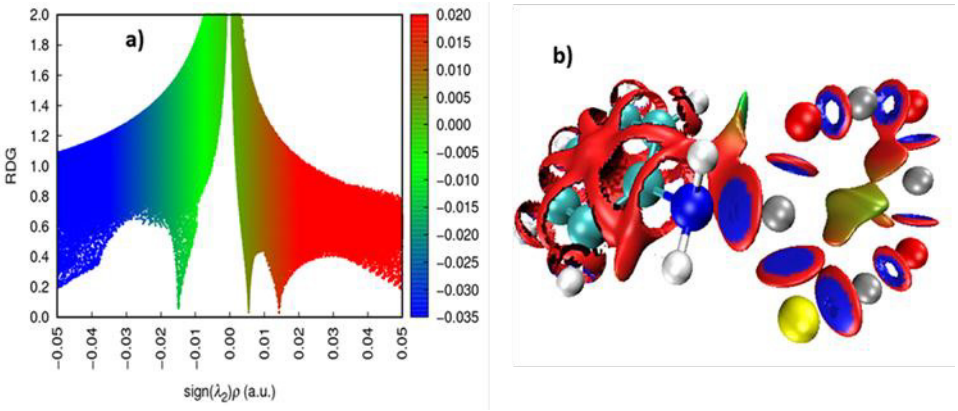

Fig. 3. NCI analysis of aniline adsorbed on the ZnO-ZnS surface.(a) RDG scatter plot showing reduced density gradient *vs*. sign(λ_2)·ρ. The central green spike indicates dominant dispersion interactions; the blue shoulder corresponds to attractive electrostatic forces (e.g., N···Zn), and red regions reflect minor steric repulsion. (b) 3D NCI isosurface (RDG = 0.5 a.u.), color-coded by sign(λ_2)·ρ: blue = attractive, green = van der Waals, red = repulsive. The results highlight the complementary contributions of weak forces to the stabilization of the adsorption complex.

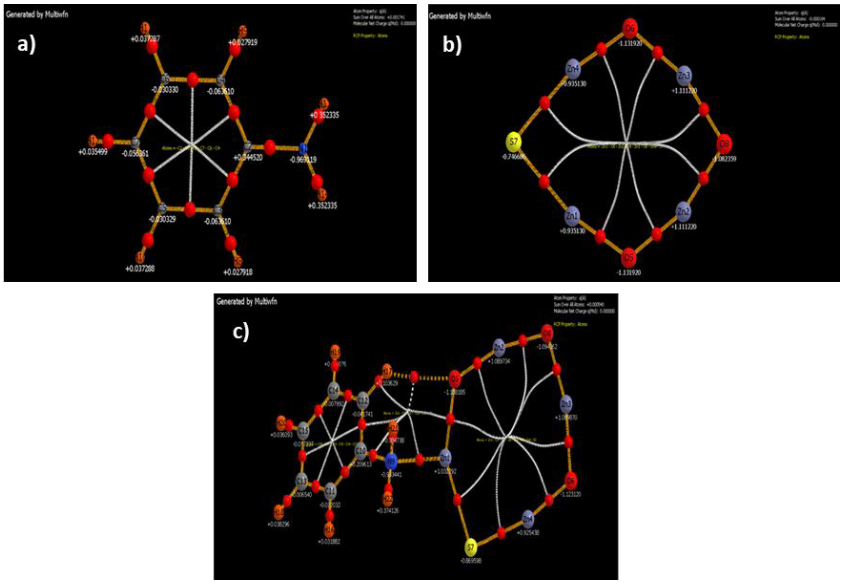

Fig. 4. QTAIM atomic graphs generated via Multiwfn: (a) Aniline molecule showing atomic charges (q(A)) and covalent bond paths. The nitrogen atom is highly negative (–0.969 a.u.), indicating lone pair availability.(b) ZnO-ZnS surface displaying Zn–O and Zn–S polar bonds. Zn atoms are positively charged, while O and S are electron-rich. (c) Aniline adsorbed on ZnO-ZnS. A new bond path is formed between the aniline nitrogen and Zn1, confirming a donor–acceptor interaction. All native bonding topologies remain intact.

between the aniline π-system and the ZnO-ZnS surface—highlighting the importance of dispersion forces in stabilizing the adsorbed geometry [18, 20]. A blue region is observed between the nitrogen atom of aniline and a nearby Zn atom, suggesting a localized, attractive donor–acceptor interaction, consistent with lone pair donation (N → Zn). This is in agreement with previous findings from ESP and ELF analyses, which showed a region of electron localization at the nitrogen site and electrostatic complementarity with positively polarized Zn centers [21, 22]. Red isosurfaces, indicating repulsive interactions, are sparse and confined to limited H···O/S contacts. Their minimal extent confirms a sterically favorable adsorption geometry, with negligible Pauli repulsion. The combination of NCI isosurface and scatter plot confirms a multi-modal interaction mechanism for aniline adsorption on the ZnO-ZnS surface: Localized attractive interactions (blue zone) signify site-specific electron donation (N → Zn), likely a Lewis acid–base interaction. Dispersive forces (green region) provide a broad, stabilizing π-surface interaction, playing a critical role in non-covalent surface anchoring [23]. Minimal steric hindrance (red zones) confirms well-optimized adsorption geometry. These findings reinforce conclusions from prior ELF and ESP analyses and highlight the importance of weak, non-covalent forces in determining the stability of hybrid organic–inorganic systems[22].

QTAIM Analysis

Fig. 4a shows QTAIM atomic graph of aniline: The QTAIM molecular graph of aniline in isolation is depicted, illustrating atomic charges (q(A)) and bond paths (indicated by solid lines) connecting atomic nuclei. The nitrogen atom (N1) carries a significant negative charge (–0.969 a.u.), which aligns with its capacity to act as a lone pair donor. The C–C bond paths constitute a continuous hexagonal structure, with bond ellipticities in the range of ~0.14–0.18, which are indicative of π-electron delocalization. All C–H and N–H bonds are characterized by elevated electron density and strong covalent character (ρ > 0.26 a.u.), as anticipated for a stable aromatic amine. Fig. 4b illustrates QTAIM atomic graph of ZnO-ZnS samples. This figure presents the surface topology of the ZnO-ZnS cluster, detailing the connectivity and charge distribution among Zn, O, and S atoms. Zinc atoms display positive charges, ranging from +0.93 to +1.11 a.u., while oxygen atoms exhibit substantial negative charges (–1.13 a.u.), and sulfur atoms show moderate negative charges (–0.75 a.u.). The presence of Zn–O and Zn–S bonds is clearly demonstrated through bond paths; these bonds are characterized by low electron density (ρ) and positive Laplacians, confirming their polar ionic nature. Fig. 4c depicts QTAIM molecular graph of aniline adsorbed on ZnO-ZnS. This detailed illustration combines the aniline molecule with the ZnO-ZnS surface, highlighting key interactions: a newly formed bond path (BCP) is observed between N9 (of aniline) and Zn1, providing evidence for a donor-acceptor interaction (ρ = 0.075 a.u., $\nabla^2\rho$ = +0.278 a.u.). The π-system of aniline maintains its ring integrity, showing no distortion or shift in the ring critical point (RCP). The persistence of all Zn–O/S bonds suggests that the surface structure remains stable following aniline adsorption.

Table 1 presents a summary of the bond characteristics observed in this study. Analysis of the topology of aniline adsorbed on the ZnO-ZnS surface reveals significant electronic rearrangement following adsorption, particularly between the nitrogen atom of aniline and the Zn1 atom located on the surface. A new bond critical point (BCP) is formed between Zn1 and N9, characterized by an electron density (ρ) of 0.075 a.u., a Laplacian of the electron density ($\nabla^2\rho$) of +0.278 a.u., and an ellipticity of 0.0487. These values suggest a non-covalent donor-acceptor interaction, typically categorized as a closed-shell electrostatic or coordinate bond.[19]. This

Table 1. Summary of bond characterization.

Bond	ρ (a.u.)	$\nabla^2\rho$ (a.u.)	Ellipticity	Nature
C–C (aromatic)	0.284–0.291	–0.67 to –0.70	0.14–0.18	Covalent with π-delocalization
N–C, N–H	0.281–0.326	–1.29	0.05–0.06	Strong covalent
Zn–O	~0.131	+0.62	~0.017	Polar covalent / ionic
Zn–S	~0.081	+0.12	~0.034	Polar covalent
Zn–N (ads.)	0.075	+0.278	0.0487	Donor–acceptor (coordinate)

finding supports previous ESP and NCI results that revealed: a negative ESP region around nitrogen (electron-rich), a positive ESP region around Zn (electron-deficient), a blue NCI region at the same N···Zn interface. The relatively low electron density (ρ < 0.1 a.u.) and positive Laplacian at the Zn–N BCP confirm the non-covalent nature of the interaction, yet indicate significant charge transfer stabilization.

Frontier molecular orbital and binding energy

Fig. 5 illustrates the optimized highest occupied molecular orbital (HOMO) and lowest unoccupied molecular orbital (LUMO) configurations for aniline, ZnO-ZnS, and the ZnO-ZnS–aniline hybrid system. To further probe the chemical behavior of the ZnO-ZnS–aniline system, including its reactivity, stability, and charge transfer properties, we calculated global conceptual DFT descriptors derived from frontier molecular orbital energies. These descriptors encompass the ionization potential (IP), electron affinity (EA), chemical potential (μ), global hardness (η), electrophilicity index (ω), and global softness (S). These results are presented in Table 2. These descriptors, rooted in conceptual DFT principles [24], offer valuable insights into the reactivity of a molecule or complex towards nucleophilic and electrophilic interactions, with their values undergoing notable changes upon adsorption.

HOMO–LUMO gap and global hardness (η): Aniline exhibits the largest HOMO–LUMO gap (5.43 eV), suggesting substantial electronic stability and limited reactivity. The ZnO-ZnS surface displays a gap of 4.23 eV, which is characteristic of wide-bandgap semiconductors [25]. The hybrid system (ZnO-ZnS–aniline) shows a significant reduction in the energy gap to 2.73 eV, indicating enhanced reactivity attributed to orbital polarization and interaction effects. Consistently, the global hardness (η = ½ ΔE) decreases across the sequence (aniline: 2.72 eV → hybrid: 1.36 eV), indicating a reduced resistance to charge transfer [26], as detailed in Table 3.

Chemical potential (μ), IP, and EA: The chemical potential (μ) becomes increasingly negative

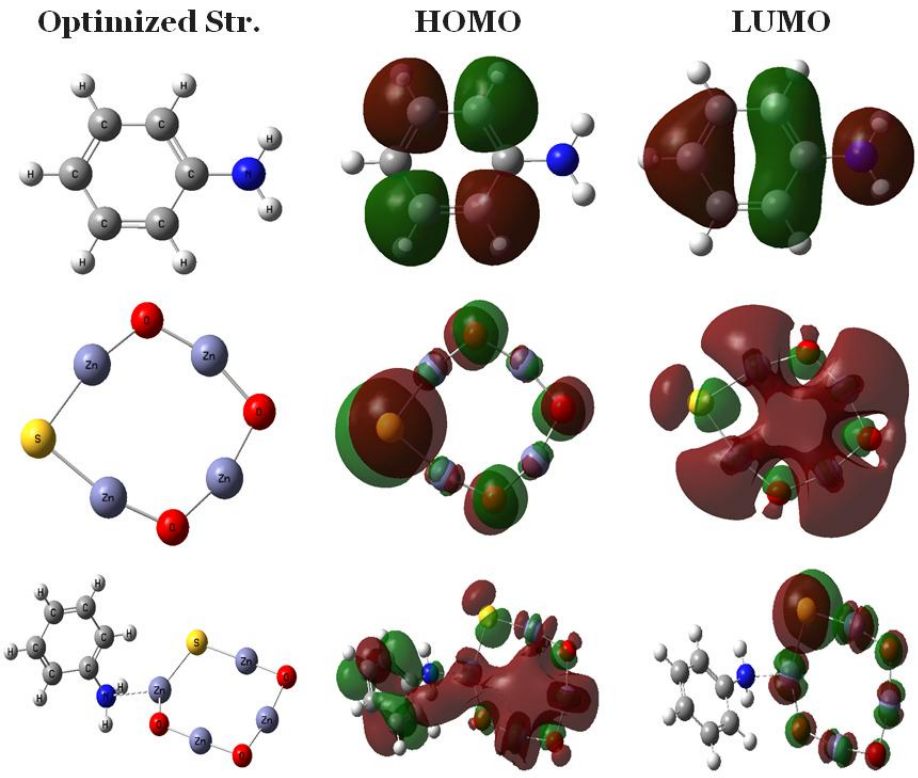

Fig. 5. Optimization, HOMO and LUMO for aniline, ZnO-ZnS and ZnO-ZnS–aniline systems.

Table 2. Some optimized quantum chemical parameters for ZnO-ZnS–aniline systems by DFT at B3LYP functional and a 6-31G(d,p) basis set for all non-metal atoms. For Zn and S, the LANL2DZ.

Substance	E_{HOMO}	E_{LUMO}	$\Delta E_{(Gap)}$	(η)	(μ)	IP	EA	(ω)	Softness
Aniline	-5.36	0.063	5.431	2.715	-2.65	5.368	-0.063	1.294	0.368
ZnO-ZnS	-6.87	-2.639	4.231	2.1156	-4.754	6.870	2.639	5.342	0.472
ZnO-ZnS–aniline	-7.476	-4.745	2.730	1.365	-6.110	7.4761	4.7451	13.672	0.732

Table 3. Trend observed for interfacial charge transfer of adsorption of aniline on surface of ZnO-ZnS nanocomposite.

Descriptor	Trend Observed	Implication
ΔE (Gap)	↓ from aniline → complex	Increased reactivity, orbital overlap
η (Hardness)	↓	Easier electron transfer
μ (Potential)	↓	Stronger electron-accepting ability
EA	↑	Enhanced LUMO stabilization
ω (Electrophilicity)	↑ (13.67 eV in complex)	System becomes highly electrophilic
S (Softness)	↑	Greater polarizability, tunable interface

upon adsorption (shifting from –2.65 eV in aniline to –6.11 eV in the hybrid), suggesting a greater electron-attracting capability. The ionization potential (IP = –EHOMO) increases substantially, rising from 5.37 eV in aniline to 7.47 eV in the hybrid, demonstrating significant HOMO stabilization. Conversely, the electron affinity (EA = –ELUMO) increases sharply from –0.06 eV (aniline) to 4.75 eV in the hybrid, indicating enhanced LUMO stabilization and an increased capacity to accept charge, a typical indicator of surface-induced polarization [27]. Electrophilicity index (ω) and global softness (S): The electrophilicity index ($\omega = \mu^2/2\eta$), which quantifies a system's ability for accepting electron density, increases from 1.29 eV (aniline) to 13.67 eV in the hybrid, suggesting a shift from a weakly to a strongly electrophilic system [28]. This is further supported by the increase in global softness ($S = 1/\eta$) [29], which nearly triples upon adsorption, consistent with enhanced electronic flexibility, as presented in Table 3.. These trends collectively indicate that aniline adsorption on ZnO-ZnS alters the overall reactivity profile, leading to increased electronic softness, enhanced charge acceptance, and greater electrophilicity. These characteristics are crucial for interfacial charge transfer processes, which are vital in surface sensing applications, catalysis, and optoelectronic devices [30].

CONCLUSION

In this study, the adsorption behavior of aniline on a ZnO-ZnS hybrid surface was investigated using a combination of ESP, ELF, and NCI analyses based on DFT calculations. These complementary methods provide a comprehensive understanding of the electronic and interaction landscape governing the stability and orientation of the adsorbed complex. QTAIM analysis reveals the formation of a bond critical point between aniline's nitrogen and a Zn atom on the surface, indicating a non-covalent donor–acceptor interaction. Frontier molecular orbital analysis shows significant spatial and energetic separation of HOMO (localized on aniline) and LUMO (on ZnO-ZnS), with a reduced band gap for the hybrid, supporting a charge-transfer adsorption mechanism. The integrated findings provide a complete electronic and topological profile of the interaction, reinforcing the importance of weak forces in adsorption and suggesting potential utility in surface-based electronic and sensing devices. Overall, these results indicate that the adsorption of aniline onto ZnO-ZnS is governed by a synergistic balance of non-covalent interactions, rather than strong covalent bonding.

CONFLICT OF INTEREST

The authors declare that there is no conflict of interests regarding the publication of this manuscript.

REFERENCES

1. Aljeboree AM, Alshirifi AN, Alkaim AF. Kinetics and

equilibrium study for the adsorption of textile dyes on coconut shell activated carbon. Arabian Journal of Chemistry. 2017;10:S3381-S3393.
2. Bento RT, Pillis MF. Titanium Dioxide Films for Photocatalytic Degradation of Methyl Orange Dye. Titanium Dioxide - Material for a Sustainable Environment: InTech; 2018.
3. Efficient Adsorption and Removal of the Herbicide 2,4-Dichlorophenylacetic Acid from Aqueous Solutions Using MIL-88(Fe)-NH_2. American Chemical Society (ACS).
4. Wang PW. Photocatalytic Degradation of Bisphenol AF in TiO_2 Suspension. Advanced Materials Research. 2014;955-959:2334-2339.
5. Taifi A, Alkadir OKA, Aljeboree AM, Al Bayaa AL, Alkaim AF, Abed SA. Environmental Removal of Reactive Blue 49 Dye From Aqueous Solution by (Lemon peels as activated carbon): a Model of Low Cost agricultural waste. IOP Conference Series: Earth and Environmental Science. 2022;1029(1):012010.
6. Yousefi S, Sadeghzadeh-Attar A. Coupling effect of Fe-doped Co3O4 nanoparticles with $SrTiO_3$ nanotubes on the high-efficiency photocatalytic activities of basic violet 16 dye degradation and H_2 evolution. Inorg Chem Commun. 2024;162:112273.
7. Jasim MS, Alaa Jasim M. Preparation of bio-nanoparticles adsorbent derivative from Iraqi date seeds for the removal of pollutants from aqueous solutions. Experimental and Theoretical NANOTECHNOLOGY. 2021:265-268.
8. Comprehensive Electro-Optical Investigation of a Ga-Doped AlN Nanowire LED for Applications in the UVC Range. American Chemical Society (ACS).
9. Kim S, An E, Oh I, Hwang JB, Seo S, Jung Y, et al. CeO_2 nanoarray decorated Ce-doped ZnO nanowire photoanode for efficient hydrogen production with glycerol as a sacrificial agent. Catalysis Science & Technology. 2022;12(18):5517-5523.
10. Mandal SK, Paul S, Datta S, Jana D. Nitrogenated CQD decorated ZnO nanorods towards rapid photodegradation of rhodamine B: A combined experimental and theoretical approach. Appl Surf Sci. 2021;563:150315.
11. Yuvaraj S, Fernandez AC, Sundararajan M, Dash CS, Sakthivel P. Hydrothermal synthesis of ZnO–CdS nanocomposites: Structural, optical and electrical behavior. Ceram Int. 2020;46(1):391-402.
12. Liu L, Wang L, Sun D, Sun X, Liu L, Zhao W, et al. ZnO-ZnS Heterostructure as a Potent Photocatalyst in the Preparation of Some Substituted Chromenes and Remarkable Antigastrointestinal Cancer Activity. ACS omega. 2023;8(46):44276-44286.
13. Chang Y-C. Complex ZnO/ZnS nanocable and nanotube arrays with high performance photocatalytic activity. J Alloys Compd. 2016;664:538-546.
14. Drissi M, Benhalima N, Megrouss Y, Rachida R, Chouaih A, Hamzaoui F. Theoretical and experimental electrostatic potential around the m-nitrophenol molecule. Molecules (Basel, Switzerland). 2015;20(3):4042-4054.
15. Herschlag D. Faculty Opinions recommendation of Zinc coordination geometry and ligand binding affinity: the structural and kinetic analysis of the second-shell serine 228 residue and the methionine 180 residue of the aminopeptidase from Vibrio proteolyticus. Faculty Opinions – Post-Publication Peer Review of the Biomedical Literature: H1 Connect; 2008.
16. Silvi B, Savin A. Classification of chemical bonds based on topological analysis of electron localization functions. Nature. 1994;371(6499):683-686.
17. Popelier PLA, Logothetis G. Characterization of an agostic bond on the basis of the electron density. J Organomet Chem. 1998;555(1):101-111.
18. Johnson ER, Keinan S, Mori-Sánchez P, Contreras-García J, Cohen AJ, Yang W. Revealing noncovalent interactions. Journal of the American Chemical Society. 2010;132(18):6498-6506.
19. Lu T, Chen F. Multiwfn: A multifunctional wavefunction analyzer. J Comput Chem. 2011;33(5):580-592.
20. Gutiérrez-Flores J, H Huerta E, Cuevas G, Garza J, Vargas R. Revealing the Role of Noncovalent Interactions on the Conformation of the Methyl Group in Tricyclic Orthoamide. The Journal of organic chemistry. 2024;89(1):257-268.
21. Murray JS, Politzer P. The electrostatic potential: an overview. WIREs Computational Molecular Science. 2011;1(2):153-163.
22. Edgecombe KE, Becke AD. Cr2 in density-functional theory: approximate spin projection. Chem Phys Lett. 1995;244(5-6):427-432.
23. Grimme S. Density functional theory with London dispersion corrections. WIREs Computational Molecular Science. 2011;1(2):211-228.
24. Parr RG, Pearson RG. ChemInform Abstract: Absolute Hardness: Companion Parameter to Absolute Electronegativity. Chemischer Informationsdienst. 1984;15(13).
25. Belghiti ME, Bouazama S, Echihi S, Mahsoune A, Elmelouky A, Dafali A, et al. Understanding the adsorption of newly Benzylidene-aniline derivatives as a corrosion inhibitor for carbon steel in hydrochloric acid solution: Experimental, DFT and molecular dynamic simulation studies. Arabian Journal of Chemistry. 2020;13(1):1499-1519.
26. Fedorov IA, Zhuravlev YN, Berveno VP. Electronic structure and chemical bond in naphthalene and anthracene. Physical Chemistry Chemical Physics. 2011;13(13):5679.
27. Arivazhagan M, Jeyavijayan S. Vibrational spectroscopic, first-order hyperpolarizability and HOMO, LUMO studies of 1,2-dichloro-4-nitrobenzene based on Hartree–Fock and DFT calculations. Spectrochimica Acta Part A: Molecular and Biomolecular Spectroscopy. 2011;79(2):376-383.
28. Index of subjects, 1922. Journal of the Chemical Society, Transactions. 1922;121:2936.
29. Mbonu IJ, Ekereke EE, Gber TE, Iyen C, Hossain I, Egah GO, et al. Quantum capacitances of transition metal-oxides (CoO, CuO, NiO, and ZnO) doped graphene oxide nanosheet: Insight from DFT computation. Chemical Physics Impact. 2024;8:100439.
30. Miar M, Shiroudi A, Pourshamsian K, Oliaey AR, Hatamjafari F. Theoretical investigations on the HOMO–LUMO gap and global reactivity descriptor studies, natural bond orbital, and nucleus-independent chemical shifts analyses of 3-phenylbenzo[d]thiazole-2(3H)-imine and its para -substituted derivatives: Solvent and substituent effects. Journal of Chemical Research. 2020;45(1-2):147-158.